Science
AAAS

Supplementary Materials for

Connectomic comparison of mouse and human cortex

Sahil Loomba *et al*.

Corresponding author: Moritz Helmstaedter, mh@brain.mpg.de

Science **377**, eabo0924 (2022)
DOI: 10.1126/science.abo0924

The PDF file includes:

Materials and Methods
Supplementary Text
Figs. S1 to S4

Other Supplementary Material for this manuscript includes the following:

MDAR Reproducibility Checklist

Materials and Methods

Alignment of datasets

Human STG (H5), human IFG (H6), macaque (STG) and mouse (A2) SBEM datasets were aligned with Voxelytics (scalable minds, Postdam, Germany), which implements a least-squares optimization of SIFT feature matches. It minimizes the match distances for neighboring tiles in the 3D tile grid in multiple steps, first using translation only, then one affine transformation per tile, and finally fine-grained mesh transforms. It also includes several heuristics to exclude false matches, including RANSAC optimization (88).

Volumetric model of synapse and axon types

The model used to obtain classification criteria for inhibitory vs. excitatory axons (Figures 4B-E) was defined as follows. To analyze synaptic inputs onto spiny and smooth dendrites (Fig. 4C-E, 5I-K), it was assumed that the cortical volume contains two distinct axon populations: excitatory axons and inhibitory axons. The two axon populations were assumed to differ in prevalence and potentially also in synapse densities. As a result, it was assumed that the fraction of excitatory synapses in the cortical neuropil was p_{exc}.
Furthermore, it was assumed that excitatory and inhibitory axons differed in the fraction of synapses established onto spine heads (of spiny dendrites), onto shafts of spiny dendrites, and onto shafts of smooth dendrites.

The probabilities of an inhibitory axon to innervate spine heads (p_{inh}^{spine}), shafts of spiny dendrites ($p_{inh}^{spiny\ shaft}$), or shafts of smooth dendrites ($p_{inh}^{smooth\ shaft}$) were assumed to be constant across interneurons and constant along individual interneuron axons. Additionally, the targets of synapses along inhibitory axons were assumed to be independent. Together, these assumptions allowed inhibitory axons to be modeled by a multinomial distribution.

For excitatory axons, it was observed that the prevalence of postsynaptic target changes with distance to soma (Fig. 3H,I). To account for this, excitatory axons were modeled by a Dirichlet-multinomial distribution with parameters $\alpha_{exc} = \left(\alpha_{exc}^{spine}, \alpha_{exc}^{spiny\ shaft}, \alpha_{exc}^{smooth\ shaft}\right)$.

Data and parameter inference

To analyze the neuropil composition, five types of measurements were taken:

1. In boxes of cortical neuropil (average total volume per dataset: 375µm^3 for mouse, 1200µm^3 for primate), the number of synapses onto spine heads and the number of synapses onto dendritic shafts were measured (average total number of synapses per dataset: 338 for mouse, 322.8 for primate). For macaque S1 and human STG, the shaft synapses were further subdivided into shaft synapses onto spiny dendrites and into shaft synapses onto smooth dendrites.
2. Along distal segments of spiny dendrites (minimum distance from soma: 30µm for mouse, 45µm for macaque, 80µm for human), the number of synapses onto spine heads and the number of synapses onto dendritic shafts were measured (average number of dendrites and of synapses per dendrite: 9.2 and 23.3 per mouse dataset, 21.2 and 17.1 per primate datasets).
3. Random spine synapses onto distal pyramidal neuron dendrites were used as “seeds” for the local reconstruction of the presynaptic axon and its postsynaptic targets (average number of axons and of synapses per axon: 13.8 and 8.4 per mouse dataset, 21.8 and 6.9 per primate dataset).

4. As in 3, but with shaft synapses onto distal spiny dendrites as (average number of axons and of synapses per axon: 16.8 and 7.7 per mouse dataset, 34.8 and 8.9 per primate dataset).
5. As in 3, but with shaft synapses onto distal dendrites of inhibitory interneurons (minimum distance from soma: 30 μm) as seeds (average number of axons and of synapses per axon: 47 and 8.1 per mouse dataset, 35 and 6.3 per primate dataset).

Synapses onto other postsynaptic targets (e.g., spine necks) were ignored. From these data, the maximum likelihood estimates of the parameters p_{exc}, α_{exc}^{spine}, $\alpha_{exc}^{spiny\ shaft}$, $\alpha_{exc}^{smooth\ shaft}$, p_{inh}^{spine}, $p_{inh}^{spiny\ shaft}$, and $p_{inh}^{smooth\ shaft}$ were derived. The likelihood was given by:

$$\mathcal{L} = \mathcal{L}_{vol.} \times \mathcal{L}_{sp.\ dend.} \times \mathcal{L}_{spine-seeded\ ax.} \times \mathcal{L}_{spiny\ shaft-seeded\ ax.} \times \mathcal{L}_{smooth\ shaft-seeded\ ax.}$$

$$\mathcal{L}_{vol} = \prod_{b=1}^{N_{boxes}} \text{Binomial}\left(V_b^{spine} \middle| V_b^{all}, p_{vol}^{spine}\right),$$

where $p_{vol}^{spine} = p_{exc}p_{exc}^{spine} + (1 - p_{exc})p_{inh}^{spine}$
and $p_{exc}^{t} = \alpha_{exc}^{t} / \|\boldsymbol{\alpha_{exc}}\|_1$ for all targets.

$$\mathcal{L}_{spiny\ dend.} = \prod_{d=1}^{N_{spiny\ dend.}} \text{Binomial}\left(D_d^{spine} \middle| D_d^{all}, p_{spiny\ dend}^{spine}\right),$$

where $p_{spiny\ dend}^{spine} = \dfrac{p_{exc}p_{exc}^{spine} + (1 - p_{exc})p_{inh}^{spine}}{p_{exc}\left(p_{exc}^{spine} + p_{exc}^{spiny\ shaft}\right) + (1 - p_{exc})\left(p_{inh}^{spine} + p_{inh}^{spiny\ shaft}\right)}$

$$\mathcal{L}_{spine-seeded\ ax.} = \prod_{a=1}^{N_{axons}} \left[f_{exc} \frac{A_a^{spine}\ \text{BetaBinomial}\left(A_a^{spine} \middle| A_a^{all}, \alpha_{exc}^{spine}, \alpha_{exc}^{spiny\ shaft} + \alpha_{exc}^{smooth\ shaft}\right)}{A_a^{all} p_{exc}^{spine}} + \left(1 - f_{exc}\right) \frac{A_a^{spine}\ \text{Binomial}\left(A_a^{spine} \middle| A_a^{all}, p_{inh}^{spine}\right)}{A_a^{all} p_{inh}^{spine}} \right],$$

where $f_{exc} = \dfrac{p_{exc}p_{exc}^{spine}}{p_{exc}p_{exc}^{spine} + (1 - p_{exc})p_{inh}^{spine}}$

$$\mathcal{L}_{spiny\ shaft-seeded\ ax.} = \prod_{a=1}^{N_{axons}} \left[f_{exc} \sum_{n=0}^{B_a^{shaft}} \frac{n\ \text{DirichletMultinomial}(B_a^{spine}, n, B_a^{shaft} - n | \boldsymbol{\alpha_{exc}})}{B_a^{all} p_{exc}^{spiny\ shaft}} + \left(1 - f_{exc}\right) \sum_{n=0}^{B_a^{shaft}} \frac{n\ \text{Multinomial}(B_a^{spine}, n, B_a^{shaft} - n | \boldsymbol{p_{inh}})}{B_a^{all} p_{inh}^{spiny\ shaft}} \right],$$

where $f_{exc} = \dfrac{p_{exc}p_{exc}^{spiny\ shaft}}{p_{exc}p_{exc}^{spiny\ shaft} + \left(1 - p_{exc}\right)p_{inh}^{spiny\ shaft}}$

$$\mathcal{L}_{smooth\ shaft-seeded\ ax.}$$
$$= \prod_{a=1}^{N_{axons}} \left[f_{exc} \sum_{n=0}^{C_a^{shaft}} \frac{n\,\mathrm{DirichletMultinomial}(C_a^{spine}, C_a^{shaft}-n, n|\boldsymbol{\alpha_{exc}})}{C_a^{all} p_{exc}^{smooth\ shaft}} + (1-f_{exc}) \sum_{n=0}^{C_a^{shaft}} \frac{n\,\mathrm{Multinomial}(C_a^{spine}, C_a^{shaft}-n, n|\boldsymbol{p_{inh}})}{C_a^{all} p_{inh}^{smooth\ shaft}} \right],$$

where $f_{exc} = \dfrac{p_{exc} p_{exc}^{smooth\ shaft}}{p_{exc} p_{exc}^{smooth\ shaft} + (1-p_{exc}) p_{inh}^{smooth\ shaft}}$

To compute the maximum likelihood parameter estimates, the fmincon function of MATLAB (R2017b) was used to minimize the negative log-likelihood. $p_{inh}^{smooth\ shaft}$ was defined as $1 - p_{inh}^{spine} - p_{inh}^{spiny\ shaft}$. The parameters were constrained as follows: $0.5 < p_{exc} < 1$, $0 < p_{inh}^{spine} < 0.5$, $0 < p_{inh}^{spiny\ shaft} < 1$, $p_{inh}^{spine} + p_{inh}^{spiny\ shaft} < 1$, $0 < \alpha_{exc}^{t}$ for all targets, and $\alpha_{exc}^{spiny\ shaft} + \alpha_{exc}^{smooth\ shaft} < \alpha_{exc}^{spine}$. The parameters were initialized to $p_{exc} = 90\%$, $p_{inh}^{spine} = 20\%$, $p_{inh}^{spiny\ shaft} = 40\%$, $\alpha_{exc}^{spine} = 9$, $\alpha_{exc}^{spiny\ shaft} = 1.5$, $\alpha_{exc}^{smooth\ shaft} = 1.5$.

The expected fraction of synapses onto spiny dendrites that originate from inhibitory axons is

$$I = \frac{(1-p_{exc})(p_{inh}^{spine} + p_{inh}^{spiny\ shaft})}{(1-p_{exc})(p_{inh}^{spine} + p_{inh}^{spiny\ shaft}) + p_{exc}(p_{exc}^{spine} + p_{exc}^{spiny\ shaft})}.$$

For the quantification of uncertainty and for statistical testing, bootstrap sampling was used (99): The measurements for each of the five types of input data were resampled with replacement while keeping the number of measurements unchanged. These data were then used for inference of maximum likelihood parameter estimates and of the expected inhibitory synaptic input fractions for spiny and smooth dendrites. This process was repeated n=1000 times per dataset.

To predict how a change in the proportion of excitatory and inhibitory neurons affects I, the following model was used: Let f_i denote the fraction of (inhibitory) interneurons. It follows that the expected synapse contribution of interneurons relative to excitatory neurons is $c = [(1-f_i)I]/[f_i(1-I)]$. Assuming that the neuronal synapse contributions remain constant, a change in the fraction of inhibitory neurons to $\hat{f}_i$ results in a predicted inhibitory synaptic input fraction of $\hat{I} = c\hat{f}_i / \left[c\hat{f}_i + 1(1-\hat{f}_i)\right]$.

For statistical testing, I was computed as the average inhibitory input synapse fraction of spiny dendrites across all mouse datasets. f_i and $\hat{f}_i$ were obtained by bootstrap sampling the pooled excitatory neuron and interneuron counts across all mouse and human datasets, respectively. $\hat{I}$ was then compared against the average inhibitory input synapse fraction of spiny dendrites across all human datasets (I_{human}). To compute a p-value, this comparison was repeated across 1000 bootstrap samples. Specifically, the p-value was calculated as the fraction of bootstrap samples in which $I_{human} \geq \hat{I}$.

To validate the initial parameters of the likelihood maximization procedure, the following approach was used. Model parameters were randomly sampled: p_{exc} uniformly between 0 and 1; p_{inh}^{spine}, $p_{inh}^{spiny\ shaft}$, and $p_{inh}^{smooth\ shaft}$ uniformly from the 2-simplex; p_{exc}^{spine}, $p_{exc}^{spiny\ shaft}$, and $p_{exc}^{smooth\ shaft}$ uniformly from the 2-simplex, and $\alpha_{exc}^{total} = 10^z$ with z uniformly between -1 and +2. α_{exc}^{target} was set to $\alpha_{exc}^{total} p_{exc}^{target}$ for all targets. For each dataset, 10,000 sets of random model parameters were generated this way and evaluated in terms of the likelihood of the model input data. The random model parameters with maximum likelihood were then used as initial parameter values for the likelihood maximization procedure (as above). For all nine

datasets, the inhibitory synaptic input fractions for spiny and smooth dendrites inferred this way were identical (≥3 significant digits) to the values inferred using fixed initial model parameters.
To account for the confusion of excitatory and inhibitory synapses in macaque and human, we considered the extreme case of true inhibitory synapses getting misclassified as excitatory. This would result in the strongest under-estimation of I/(I+E) in primates. Let X = I/(I+E) denote the true inhibitory synapse fraction. Assuming that a fraction C=8.4% of true inhibitory synapses gets misclassified as excitatory (see Fig. S2), the measured inhibitory synapse fraction is (1-C)×I / [(1-C)×I + (C×I + E)] = (1-C)×I/[I+E] = (1-C)×X. Thus, the upper bound on the true value of I/(I+E) is Y / (1-C). For statistical testing, the bootstrap samples of the inhibitory synapse fractions for macaque and human were corrected as above before comparison against the predictions from mouse. We found that even the upper bound on I/(I+E) for macaque and human was significantly lower than the prediction from mouse (15.0%±1.5% vs. 24.9%±3.2%; $p<0.001$).

Connectivity estimates

The connectivity within and across excitatory neuron (ExN) and inhibitory interneuron (IN) populations (Suppl. Fig. 2F) was computed as follows: $p_{ExN\to ExN} = p_{exc}\left(p_{exc}^{spine} + p_{exc}^{spiny\ shaft}\right)$, $p_{ExN\to IN} = p_{exc}p_{exc}^{smooth\ shaft}$, $p_{IN\to ExN} = (1-p_{exc})\left(p_{inh}^{spine} + p_{inh}^{spiny\ shaft}\right)$, and $p_{IN\to IN} = (1-p_{exc})p_{inh}^{smooth\ shaft}$. For the illustration of inhibitory connectivity in Figure 6C, IN→ExN connections were established with probability $kp_{IN\to ExN}/[f_i(1-f_i)]$ and IN→IN connections with probability $kp_{IN\to IN}/f_i^2$, where f_i is the interneuron fraction and k is a constant, such that each IN innervates on average 30% of all other neurons. Notably, it was assumed that the average number of synapses in IN→ExN and IN→IN connections is equal.

Dense reconstruction

For the analyses reported in Figures 3D-F, 5G, the following methods were employed. 3D EM Datasets were processed using voxelytics (Scalable minds, Potsdam, Germany, developed in collaboration with MPI Brain Research, Dept. of Connectomics). Briefly, a convolutional neural network (CNN; modified from (54)) was used to infer voxel-wise affinities from which an initial volume segmentation was generated by seeded watershed transform. For the reconstruction of neurites, volume segments were grouped into agglomerates by median-affinity-based hierarchical agglomeration with additional constraints to reduce the rate of merge errors. These constraints include: i) neurite type-based restrictions to avoid merge errors between, for example, axons and dendrites; ii) a restriction to avoid merge errors between cells whose cell body is located within the image volume; and iii) agglomerate volume-based restrictions. Neurite types were inferred using a CNN for voxel-wise semantic segmentation of axons, dendrites, spine heads, astrocytes, myelin, and other objects. For connectome inference, a CNN for semantic segmentation of synapses, vesicle clouds, and mitochondria was used in combination with a decision tree forest that was trained to classify agglomerate-to-agglomerate contacts as synaptic or non-synaptic based on summary statistics of the CNN outputs. The CNNs and decision tree forests were trained on previously published training data from layer 4 of mouse S1 (49) and, optionally, on additional dataset-specific training data.

To separate axonal, dendritic, and other (e.g., glial) agglomerates, the volume-weighted average of voxel-wise neurite type probabilities were computed. Agglomerates were classified as axonal or dendritic if they exceeded dataset-specific axon and dendrite probability thresholds (see below), respectively. Automatically detected synapses were classified into spine synapses,

shaft synapses, and other synapses based on the average type probabilities at the postsynaptic site. Spine synapses were further sub-classified into spine synapses into singly vs. multiply innervated spine heads. For subsequent analyses, only spine synapses onto singly innervated spine heads and shaft synapses with presynaptic axon and postsynaptic dendrite agglomerates were considered.

Estimation of error rates

To estimate error rates of the automated reconstructions and to optimize analysis parameters, ground truth annotations were generated for each dataset. The ground truth consisted of synapse annotations in neuropil volumes of (5 μm)^3 for mouse, (7 μm)^3 for macaque, and (7 μm)^3 for human. Synapses were classified into spine synapses, shaft synapses, and other synapses. The postsynaptic dendrites were classified as either spiny or smooth. For spine synapses, the corresponding dendrite was identified.
The following parameters and error rates were estimated from these annotations:

- Minimum axon probability for axon agglomerates (manually optimized for high recall based on the axon probability distribution across agglomerates presynaptic to ground truth synapse annotations)
- Minimum dendrite probability for dendrite agglomerates (as for axons)
- Average automated spine synapse fractions for dendrite agglomerates corresponding to spiny (p_{spiny}^{spine}) and smooth dendrites (p_{smooth}^{spine}), respectively
- Precision and recall of automated spine synapse detection and confusion rate of true spine synapses as shaft synapses
- Precision and recall of automated shaft synapse detection and confusion rate of true shaft synapses as spine synapses

Inference of axonal spine targeting probability

To classify axon agglomerates as excitatory or inhibitory, the model of excitatory and inhibitory axons derived from manual annotations was reused (see above). Specifically, each axon agglomerate was classified based on its spine targeting probability. First, the number of automatically detected spine (N_{spine}) and shaft synapses (N_{shaft}) was computed. To account for the error rates of automated synapse detection, the normalized likelihood $\mathcal{L}_{axon}^{spine}(p_{spine}) = \mathrm{P}(N_{spine}, N_{shaft}|p_{spine})$ was estimated was follows:
For a given p_{spine}, the effect of imperfect synapse detection was simulated by a forward model for all axon configurations $n_{spine} \sim \mathrm{Binomial}(n_{total}, p_{spine})$ with $n_{total} \in [0{,}100]$. The un-normalized likelihood of p_{spine} was then approximated by the probability mass corresponding to the combination of N_{spine} and N_{shaft} after the forward model. The forward model was evaluated for $p_{spine} = 0\%, 1\%, \ldots, 100\%$. For details, see MATLAB function +HNHP/+Auto/+inferSpineSynapseFraction.m.

Given the likelihood $\mathrm{P}(N_{spine}, N_{shaft}|p_{spine})$ and the model of excitatory and inhibitory neurons, the posterior probability of being excitatory or inhibitory was computed for each axon agglomerate. For subsequent analyses, inhibitory axon agglomerates were defined as axon agglomerates with a posterior probability of being inhibitory above 50%.

Inference of smooth dendrite targeting probability for inhibitory axons

To compute the smooth dendrite targeting probability of inhibitory axons, spiny and smooth dendrites had to be separated. For a dendrite with N_{spine} input synapses onto spine

heads and N_{shaft} input synapses onto the dendritic shaft, the probability of being a smooth dendrite was computed by:

$$p_{dend}^{spiny} = \frac{\text{Binomial}(N_{spine}|N_{spine}+N_{shaft}, p_{spiny}^{spine})}{\text{Binomial}(N_{spine}|N_{spine}+N_{shaft}, p_{spiny}^{spine}) + \text{Binomial}(N_{spine}|N_{spine}+N_{shaft}, p_{smooth}^{spine})}$$

The smooth dendrite targeting probability of inhibitory axons was then computed by:

$$p_{axon}^{smooth} = 1 - \arg\max_{p_{axon}^{spiny}} \int_{p_{axon}^{spine|spiny}} \mathcal{L}_{axon}^{spine}\left(p_{axon}^{spiny} p_{axon}^{spine|spiny}\right) \prod_{\substack{postsynaptic \\ dendrites}} \left[\hat{p}_{axon}^{spiny} p_{dend}^{spiny} + (1 - \hat{p}_{axon}^{spiny})(1 - p_{dend}^{spiny})\right]$$

where p_{axon}^{spiny} is the true probability of targeting spiny dendrites, $p_{axon}^{spine|spiny}$ is the true spine synapse fraction among synapses onto spiny dendrites, and $\hat{p}_{axon}^{spiny}$ is the expected probability of targeting spiny dendrites when accounting for the error rates of automated spine and shaft synapse detection. Notably, the transformation of the former two parameters into the latter is based on the assumption that smooth dendrites are devoid of spines. For details, see MATLAB script +HNHP/+Auto/runAnalysis.m.

Supplementary Text

Possible effect of temperature on stability of dendritic spines

Reports about a temperature-dependent change in spine rates, shown for slices of mammalian hippocampus (73), could be of concern as a potential contributor to the observed low spine rates in human cortex (Fig. 2E). While our tissue was immersed in cooled liquid, this liquid was fixative in our case, which would quickly halt any additional modifications of the neuropil; in fact, we saw no evidence of ultrastructural change in macaque and H5 that has been described as a corollary of temperature-induced tissue alterations (73). Sample H6 showed occasional dendrites with swellings (beady morphology), which were excluded from analyses. Control experiments using cold fixative on mouse samples did not yield substantially altered spine rates (1.2±0.4 per µm dendrite in mouse data fixed at 4°C, n=4). Together, we have to conclude that our finding about the synaptic input to human cortical pyramidal cells should be taken to treat reports of extremely high spine rates in human (44,46) with caution (see also 29, 74, 75, 76)), even if some of the differences are attributable to variations between cortical areas in human and primates (46, 75, 77), but similar variability was not reported in mouse (55).

Additional methodological acknowledgements

We thank T. Garbowski and D. Lechner at Zeiss team for help with setting up multiSEM; M. Fahland and N. Prager at Fraunhofer FEP, Dresden for collaboration on Kapton tape; R. Schalek and J. Lichtman at Harvard University for initial advice on setting up ATUM; G. Tushev for ATUM software; and A. Kotowicz and T. Zeller for initial setup of data transfer line from multiSEM.

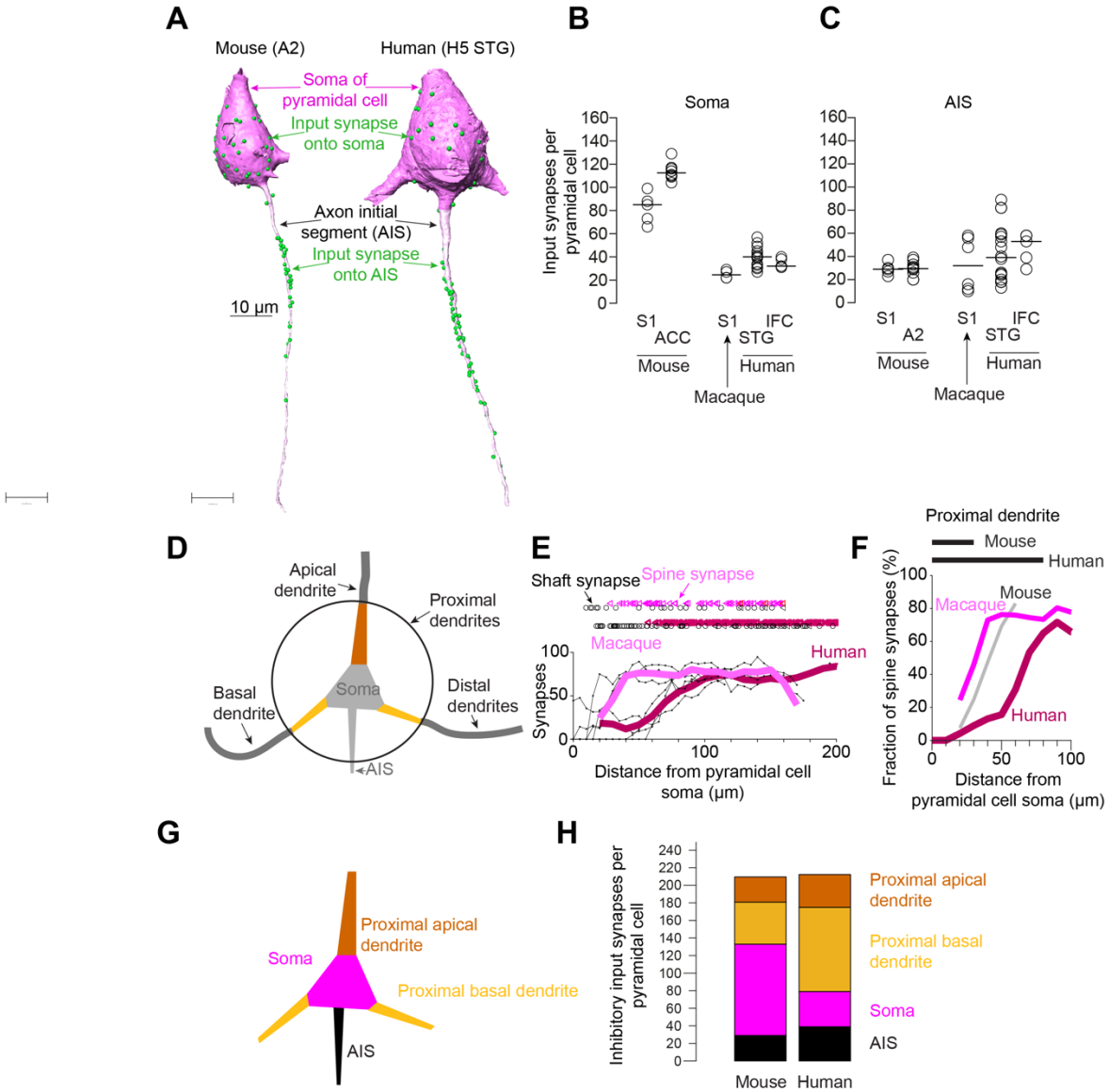

Fig. S1: Synaptic input to pyramidal cells at their soma, axon initial segment and proximal dendrites. (A) Example reconstructions of pyramidal cell bodies and axon initial segments (AIS) from mouse A2 and Human STG datasets. All input synapses to soma and AIS were manually annotated (green). Note sparsity of somatic input synapses in human. **(B,C)** Quantification of total input synapses onto soma and AIS per neuron in mouse, macaque and human. Note 2.9-fold drop of somatic input from mouse to macaque and human (104 ± 17 input synapses, N=17 somata in mouse to 36 ± 9 input synapses, N=22 somata in macaque and human, mean ± s.d., p-value<0.001, Kolmogorov-Smirnov test, B), while input to AIS is only slightly enhanced (40% increase, 29 ± 6 input synapses, N=15 AIS in mouse vs. 42 ± 23 input synapses, N=29 AIS in macaque and human, mean ± s.d., p-value<0.01, Kolmogorov-Smirnov test, C). **(D-F)** Analysis of proximal dendritic input: definition of proximal dendrites as those with reduced input spine density. Input spine density increases to distal levels within about 30µm in mouse and about 80µm in human (F), which were used as thresholds for definition of proximal dendrites in G,H. **(G,H)** Quantification of total inhibitory synaptic input to proximal dendrites using total dendritic path length per neuron of these compartments (123 ± 30 µm for proximal basal, N=10 cells and 40 ± 14 µm, N=7 cells for proximal apical in mouse and 395 ± 60 µm, N=17 cells, and 121 ± 66 µm, N=21 cells in human, respectively, mean ± s.d) and shaft input synapse densities. In the proximal dendrite, 95% and 75% of shaft inputs were inhibitory in mouse and human, respectively. (I) Summary of inhibitory synaptic input to the non-distal

input domains AIS, Soma, proximal dendrites. Note that total inhibitory input in these domains is largely constant from mouse to human, with a potential shift of synapses from soma to AIS and proximal dendrites. Notably, there was no sign of an increased inhibition in Human in these input compartments (excluding compensation of the finding of largely similar distal i/(i+e) in mouse, macaque and human, Fig. 4E). All data based on expert reconstructions.

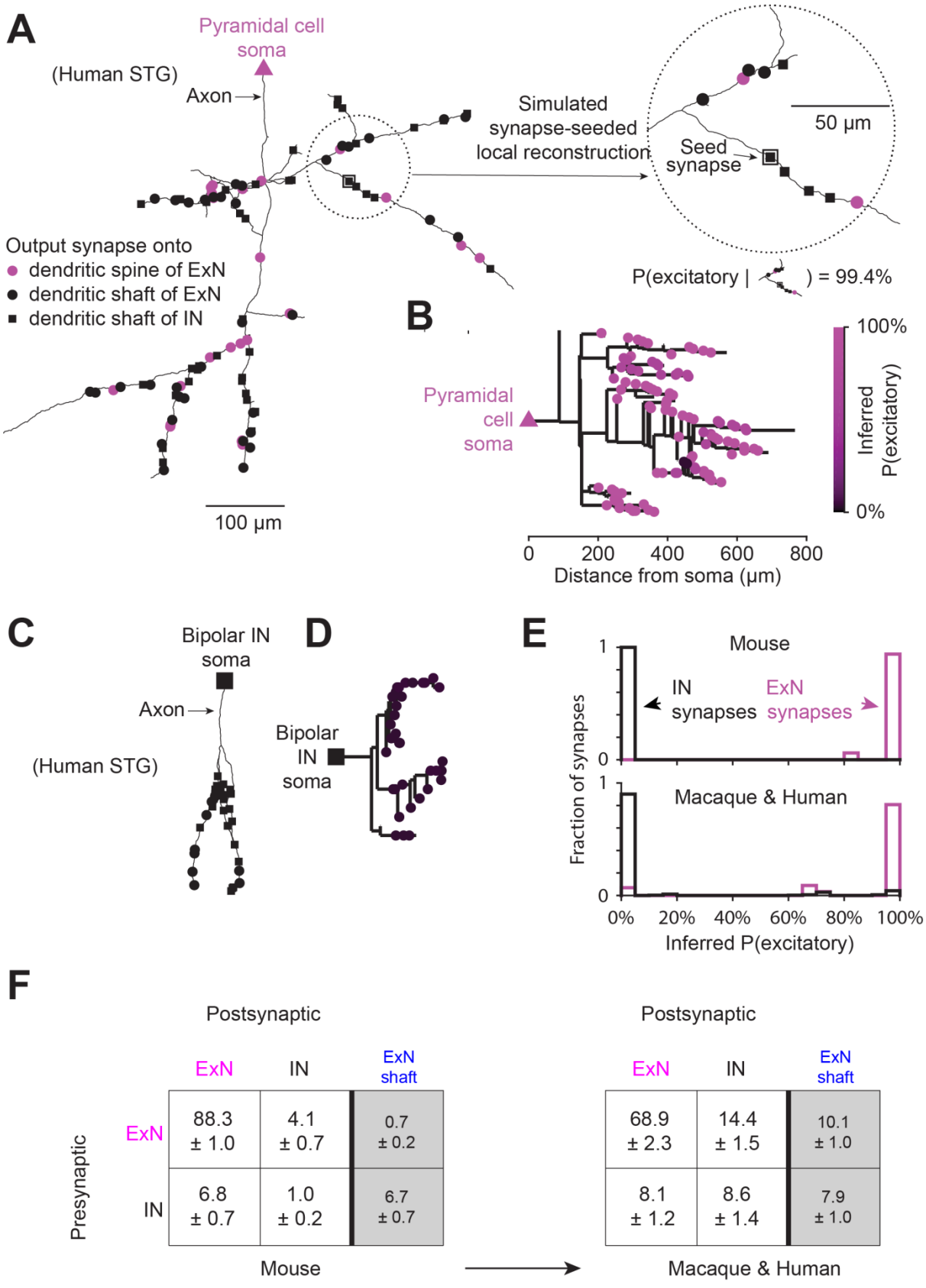

Fig. S2: Validation of excitatory and inhibitory axon definition, and network expansion. **(A)** Example pyramidal neuron axon from human STG with excitatory output synapses onto dendritic spines of excitatory neurons (ExN) (magenta circles), onto dendritic shafts of excitatory neurons (black circles), and onto dendritic shafts of interneurons (IN) (black

squares). Right: Simulation of local axon reconstruction seeded from a shaft synapse onto an IN dendrite (black square with outline). The local axon reconstruction spans the seed synapse and the nine synapses closest to it (2 onto dendritic spines, 7 onto dendritic shafts). The inferred probability of the local axon reconstruction being part of an excitatory axon is 99.4%. **(B)** Axonogram of axon in (A) with each output synapse colored by inferred excitatory probability of the corresponding simulated local reconstruction. Note that 99 out of the 101 excitatory synapses have an inferred excitatory probability >50%. **(C)** Example bipolar interneuron axon from human STG with inhibitory output synapses (symbols and scale bar as in (A)). **(D)** Axonogram of axon in (C). All 34 inhibitory synapses have an inferred excitatory probability <50%. **(E)** Histogram of inferred excitatory probability for synapses from ExN and IN axons from mouse, and macaque and human. In mouse, all 33 excitatory and 167 inhibitory synapses were correctly classified. In macaque and human, 93.1% of the 1,239 excitatory and 91.6% of the 356 inhibitory synapses were correctly classified. All data based on expert reconstructions. **(F)** Connectivity estimates from the model for mouse and macaque and human (see Suppl. Methods “Connectivity estimates”). ExN postsynaptically comprises shaft and spine targets. ExN shaft connectivity (gray shading) reported separately in rightmost column, this is part of the ExN column. Note 8.6-fold expansion of IN-to-IN connectivity, and 14.4-fold expansion of ExN connectivity at shaft synapses.

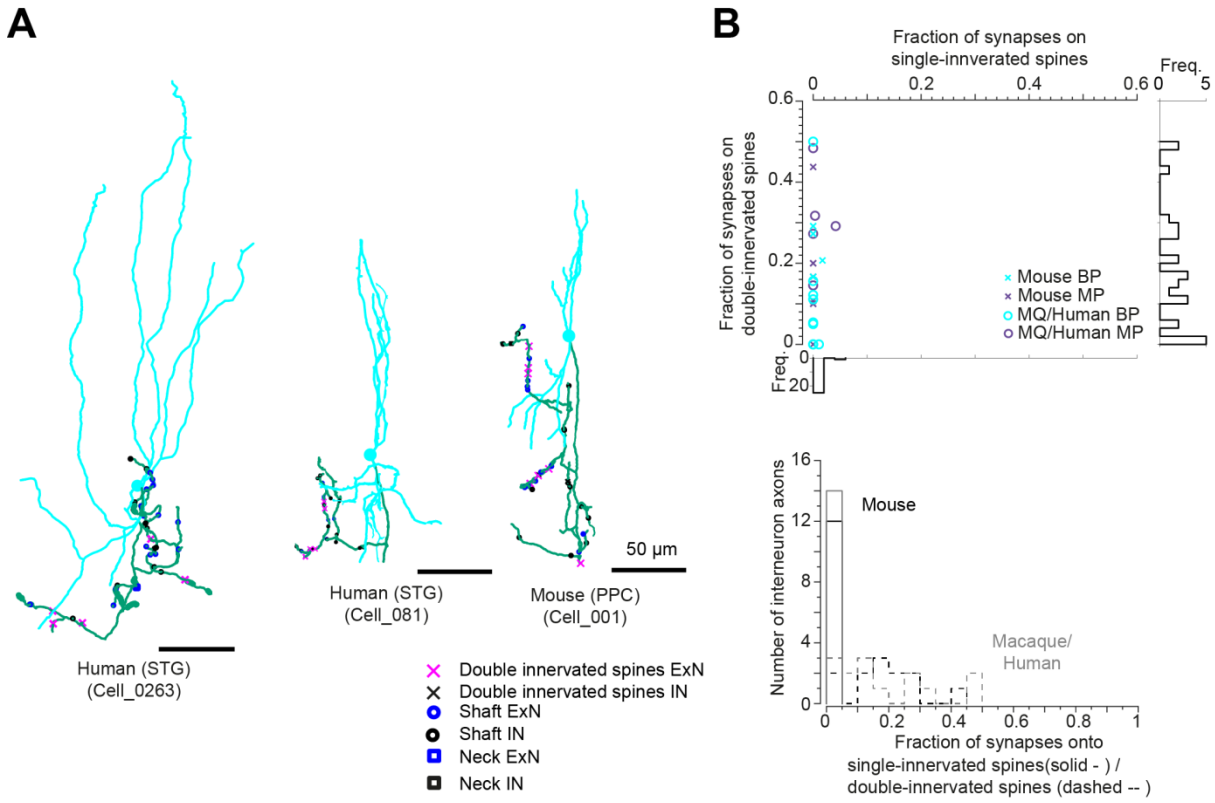

Fig. S3: Spine-targeting interneurons. (A) Example reconstructions of bipolar interneurons with output synapses onto spines, which could resemble double bouquet INs (61-63). **(B)** Quantification of spine targeting by IN axons. Note spine targeting is almost exclusively onto spines that are doubly innervated, therefore not confounding the classification of axons based on single-spine innervation (cf. Fig. 4). All data based on expert reconstructions.

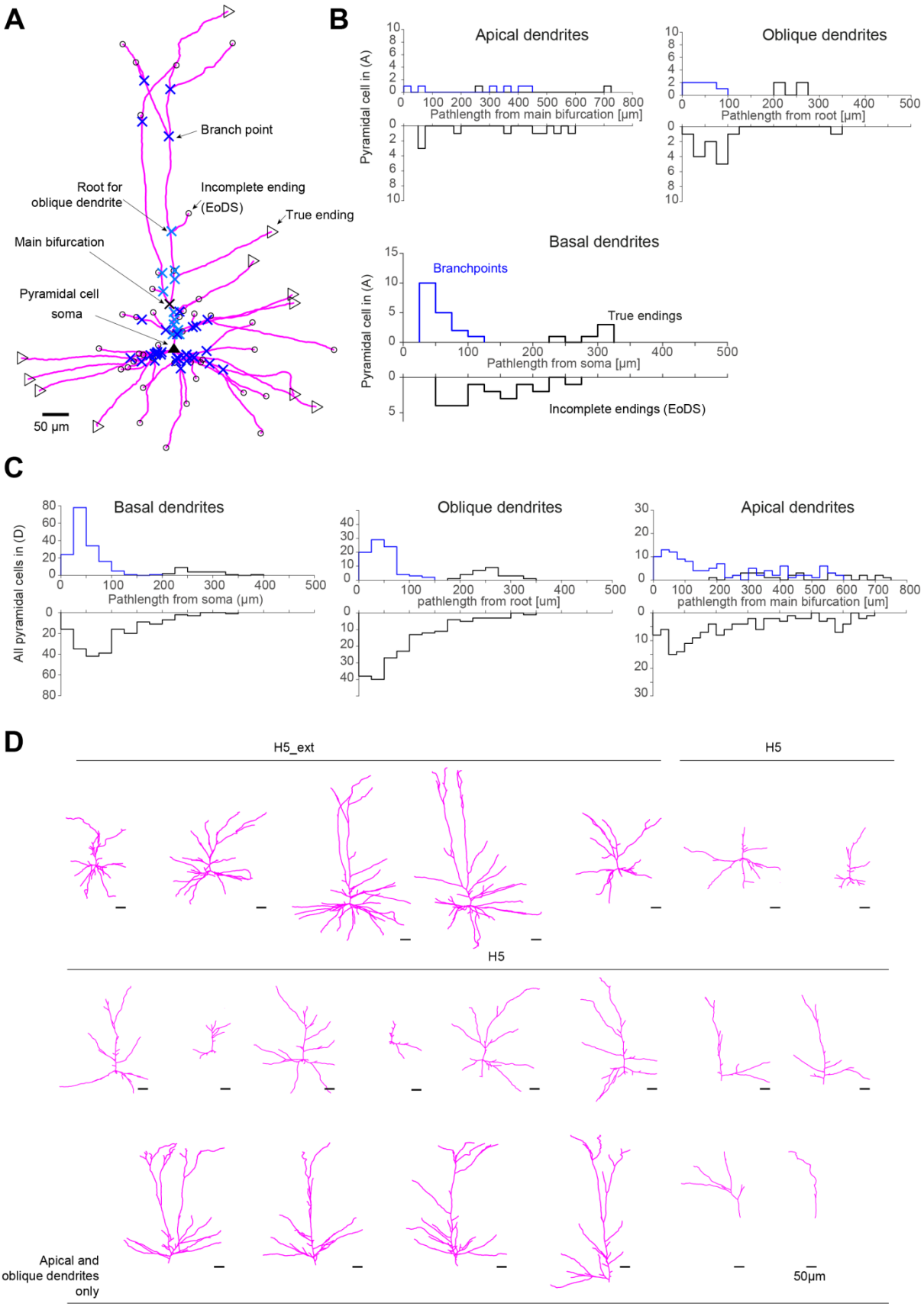

Fig. S4: Dendritic path length estimates for human pyramidal cells. (A) Example reconstruction of a dendritic tree of a L3 pyramidal cell (PC) in Human STG dataset. Dendrites were traced either until the end of the dataset (EoDs) or until an actual ending (true). **(B)** Example quantification of measured dendrite path lengths from the L3 PC shown in (A) to their

endings eods, true) and their branchpoints. Plotted separately for each compartment (apical, oblique, basal). Path lengths were either measured from the main bifurcation (apical), from the root of the apical trunk (oblique) or from the soma (basal). **(C)** Quantification of measured dendrite path lengths as shown as in (B) based on all PC reconstructions in Human STG datasets (H5, H5_ext). For the basal, oblique and apical tuft compartment N=226, 211, 167 dendrites were analyzed, of which N=25, 28 and 32 dendrites with true endings were found (N=21 cells). No EoDS ending exceeded true ending path lengths, which minimized the chance of missing longer dendrites leaving the dataset. Note the early branching especially for the basal compartment. **(D)** Reconstructions of dendritic trees of L2/3 PCs in Human STG datasets (H5 and H5_ext) with either all compartments (first and second row, n=15) or only apical compartment (below, n=6). Note that due to the smaller depth in z for the H5 dataset the PC reconstructions appear sparser than in H5_ext. Scale bars 50 µm. All data based on expert reconstructions.